Article
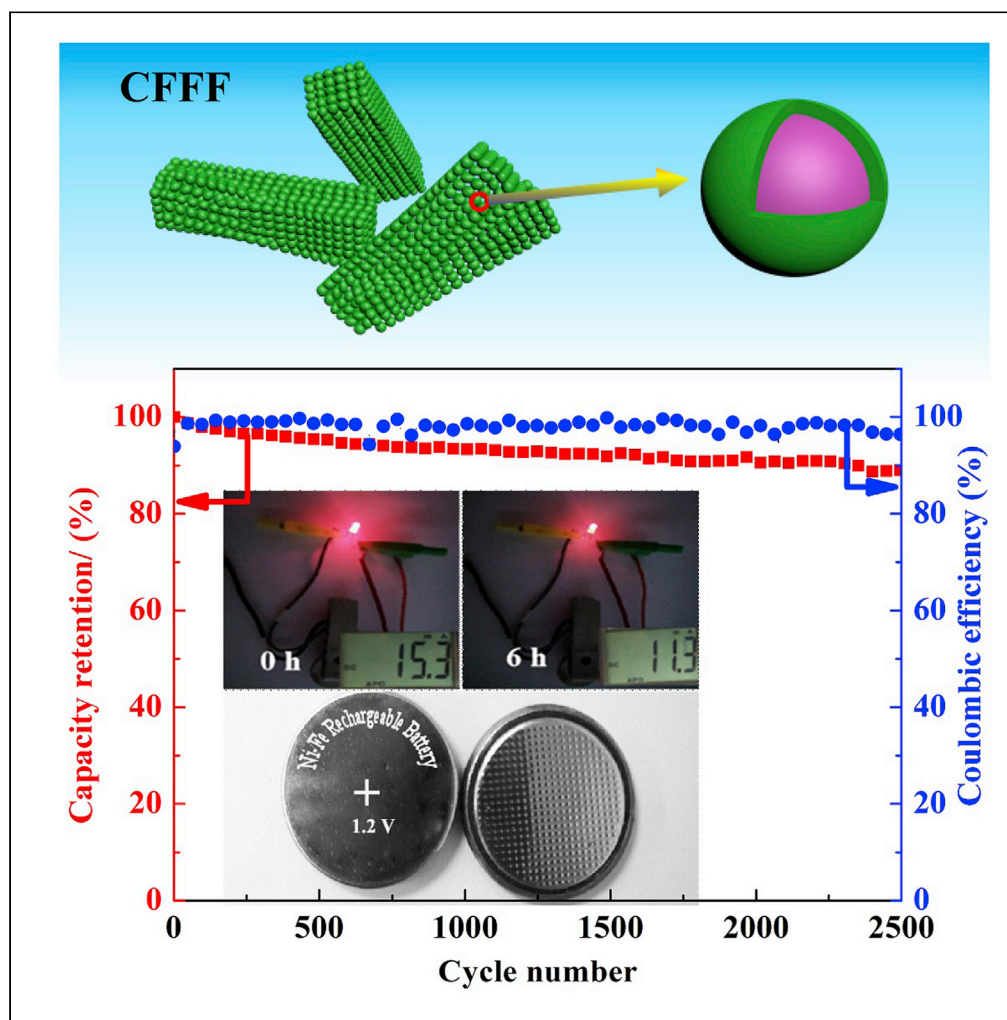
High-capacity and high-rate Ni-Fe batteries based on mesostructured quaternary carbon/Fe/FeO/Fe$_3$O$_4$ hybrid material

CFFF

Yanfei Zeng, Xinyi Zhang, Xianxing Mao, Pei Kang Shen, Douglas R. MacFarlane

xinyizhang@hubu.edu.cn (X.Z.)
douglas.macfarlane@monash.edu (D.R.M.)

Highlights

A quaternary hybrid has been fabricated by a one-step solid-state reaction.

Controlling the valence state of iron facilitates redox kinetics and charge transfer.

The hybrid anode exhibits high specific capacity of 604 mAh·g^{-1} at 1 A·g^{-1}.

The NiFe battery exhibits specific energy of 127 Wh·kg^{-1} and superior durability.

Article

High-capacity and high-rate Ni-Fe batteries based on mesostructured quaternary carbon/Fe/FeO/Fe$_3$O$_4$ hybrid material

Yanfei Zeng,[1] Xinyi Zhang,[2,*] Xianxing Mao,[1] Pei Kang Shen,[1] and Douglas R. MacFarlane[3,4,*]

SUMMARY

The Ni-Fe battery is a promising alternative to lithium ion batteries due to its long life, high reliability, and eco-friendly characteristics. However, passivation and self-discharge of the iron anode are the two main issues. Here, we demonstrate that controlling the valence state of the iron and coupling with carbon can solve these problems. We develop a mesostructured carbon/Fe/FeO/Fe$_3$O$_4$ hybrid by a one-step solid-state reaction. Experimental evidence reveals that the optimized system with three valence states of iron facilitates the redox kinetics, while the carbon layers can effectively enhance the charge transfer and suppress self-discharge. The hybrid anode exhibits high specific capacity of 604 mAh·g^{-1} at 1 A·g^{-1} and high cyclic stability. A Ni-Fe button battery is fabricated using the hybrid anode exhibits specific device energy of 127 Wh·kg^{-1} at a power density of 0.58 kW·kg^{-1} and maintains good capacity retention (90%) and coulombic efficiency (98.5%).

INTRODUCTION

There is growing demand for energy storage systems owing to the rapid development of renewable energy sources, electric vehicles, and portable electronics. Among various energy storage systems, aqueous rechargeable batteries have attracted much attention owing to their high ionic conductivity, high efficiency, low cost, and good safety characteristics (Rustomji et al., 2017; Janoschka et al., 2015; Sun et al., 2017; Guo et al., 2011). As a traditional aqueous rechargeable battery, Ni-Fe batteries have been used in various stationary and mobile applications for over a century in the USA, Europe, and Australia (Chakkaravarthy et al., 1991). Compared with the lithium ion battery, Ni-Fe batteries have the advantage of abundant material sources, being non-polluting, offering high depth of discharge, high durability and long cycle life; hence they hold great promise as large-scale electrical energy storage devices (Weinrich et al., 2018; Wu et al., 2017; Mulder et al., 2017; Lei et al., 2018; Shukla et al., 2001). As the most abundant element, an iron-based anode has high theoretical capacity, is robust, easily recycled and offers eco-friendly characteristics. However, passivation and self-discharge of iron electrodes are currently two main issues with Ni-Fe batteries. The iron electrodes in traditional devices also tend to have poor rate and cycle performance due to high self-discharge rates and hydrogen evolution during the charging-discharging (Hariprakash et al., 2005; Narayanan et al., 2017). An iron-based anode experiences up to three different valence states during the charging-discharging process. It is thought that rational design and synthesis of iron anode materials with optimized distribution of valence states could enable a substantial improvement in the electrochemical performance in Ni-Fe batteries (Li et al., 2017).

Recently, efforts have been devoted to improving the electrochemical properties of iron anodes by hybridizing iron-based materials and carbon immaterialness such as carbon nanobots and graphenes; this not only increases the conductivity and shortens the electron-transfer distances but also allows an increase in the active surface area and improves the utilization rate of the active material (Han et al., 2017; Ma et al., 2018; Li et al., 2018; Wang et al., 2012, 2019; Zhang et al., 2019; Guo and Li, 2017). However, in most cases, the preparation processes involve complex procedures, sacrificial templates, and tedious reactions. The weak physical coupling between carbon and the active materials cannot facilitate efficient charge-transfer. Besides, it is difficult to obtain a homogeneous distribution of carbon in the composites through physical blending, owing to the high hydrophobicity of nanocarbon. In this work, we report a simple one-step solid-state reaction approach for the preparation of nanostructured

[1]Collaborative Innovation Center of Sustainable Energy Materials, Guangxi Key Laboratory of Electrochemical Energy Materials, College of Chemistry and Chemical Engineering, Guangxi University, Nanning, Guangxi 530000, China

[2]Hubei Key Laboratory of Ferro- & Piezoelectric Materials and Devices, School of Physics and Electronic Science, Hubei University, Wuhan 430062, China
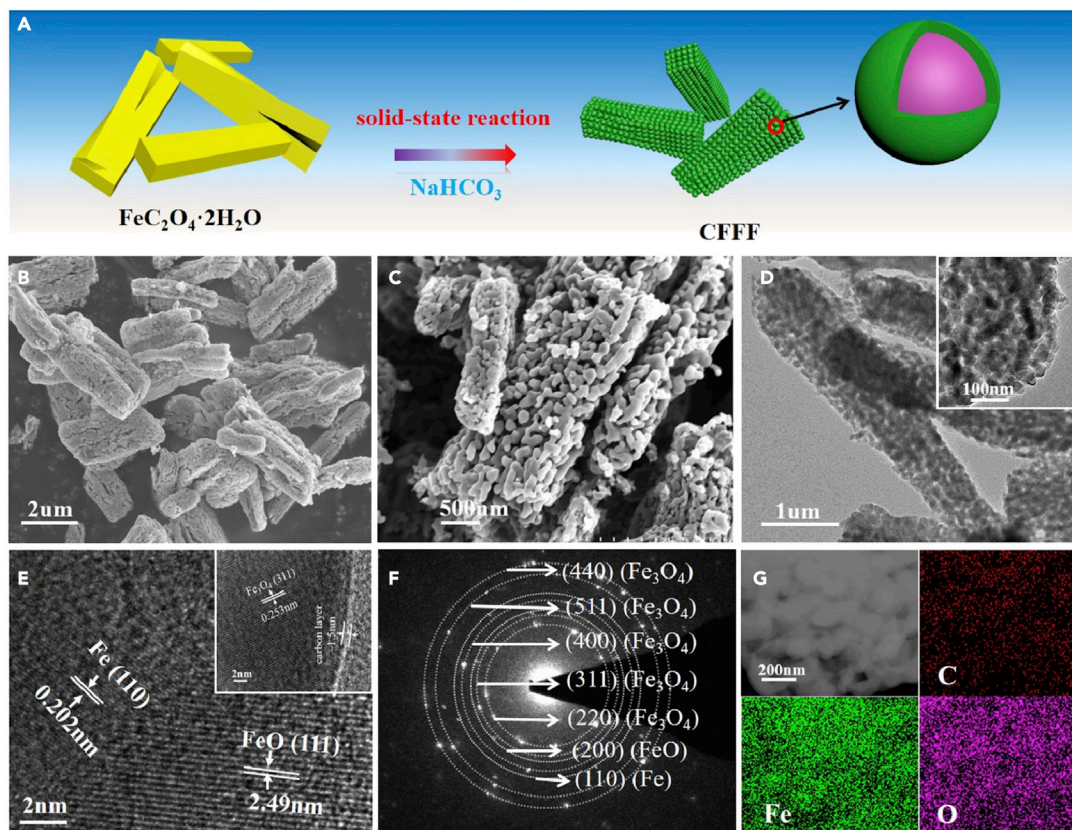
[3]ARC Centre of Excellence for Electromaterials Science, School of Chemistry, Monash University, VIC 3800, Australia

[4]Lead contact

*Correspondence:
xinyizhang@hubu.edu.cn
(X.Z.),
douglas.macfarlane@
monash.edu (D.R.M.)
https://doi.org/10.1016/j.isci.
2021.102547

Figure 1. Material characterization of CFFF-650 hybrid
(A) Schematic illustration of the formation of the CFFF.
(B) SEM.
(C) HRSEM.
(D and E)(D) TEM and (E) HRTEM images;
(F and G)(F) the corresponding electron diffraction pattern, and (G) EDS mapping images.

quaternary carbon/Fe/FeO/Fe$_3$O$_4$ (abbreviated as CFFF) hybrids with controllable composition. The CFFF composite displays not only high energy capacity but also high-rate capacity. Moreover, a CFFF-based Ni-Fe button cell exhibits ~98.5% coulombic efficiency and ~90% capacity retention after 2500 charge-discharge cycles, with a specific device energy of 127 Wh·kg^{-1} at 300 mA·g^{-1}.

RESULTS

Synthesis and characterizations of CFFF hybrid materials

CFFF was prepared by a one-step, in situ, solid-state reaction, with FeC$_2$O$_4$·2H$_2$O as precursor and NaHCO$_3$ as structure directing agent under H$_2$/Ar atmosphere (Figures 1A, S1, and S2). Figure 1B shows the SEM image of the CFFF-650. The obtained CFFF-650 possesses rod-like morphology with width and length about 1-4 μm and 5-20 μm, respectively. High-resolution SEM (HRSEM) images show that CFFF-650 is composed of assembled iron oxide nanoparticles (50-200 nm), forming uniformly distributed meso-pores (Figure 1C). With the increase of processing temperature, the pores become more pronounced (Figures S2A–SC), and the particles become finer. The pores of the CFFF rods collapse and the particle sizes increase to ~1 μm at 700°C. As shown in Figure S2D, there is no obvious porous structure in CFFF in the absence of NaHCO$_3$ under the same reaction conditions, which indicates that NaHCO$_3$ acts as the pore-forming agent during the reaction process. The transmission electron microscope (TEM) image of the CFFF-650 is shown in Figure 1D. The CFFF mesostructure is formed through the assembly of CFFF nano-particles with size ranging from tens to hundreds of nanometers. Mesoporous structure with pore size ~15 nm can be clearly observed (inset in Figure 1D). The high-resolution TEM (HRTEM) image shows
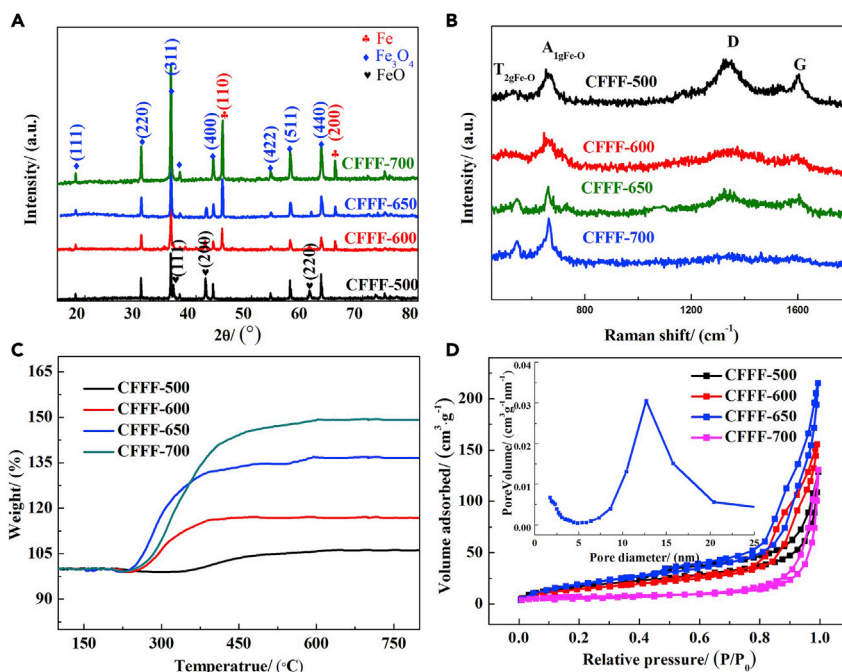
Figure 2. The XRD, Raman, TGA, and BET results of CFFF hybrids

(A) XRD patterns of CFFF hybrids and.

(B) Raman spectra of CFFF hybrids.

(C) TGA curves for the CFFF hybrids in an air atmosphere.

(D) N_2 adsorption-desorption isotherms of CFFF hybrids. The inset shows the pore size distribution plot of CFFF-650.

that CFFF nanoparticles are composed of iron oxide cores wrapped with a layer of carbon with thickness about 1.5 nm (Figure 1E). Thicker carbon layers were also observed on CFFF-500 and CFFF-600, while no carbon layer was observed on CFFF-700 (Figure S3). The lattice spaces of 0.253 nm, 0.202 nm, and 0.249 nm correspond to the (311), (110), and (111) crystal facets of spinel Fe_3O_4, body-centered cubic α-Fe and cubic FeO. The selected area electron diffraction patterns of the CFFF hybrids are shown in Figures 1F and S4. The CFFF-650 shows seven diffraction rings, corresponding to (220), (311), (400), (511), and (440) facets of cubic magnetite Fe_3O_4, (200) facets of FeO, and (110) facets of Fe, respectively. The corresponding energy-dispersive X-ray spectrometry (EDS) mapping images of aggregate (Figure 1G) and single nanoparticles (Figure S5) of CFFF clearly show a continuous uniform distribution of elements C, Fe, and O in the sample, indicating the homogeneity of the CFFF composite structure.

Figure 2A shows the X-ray diffraction (XRD) patterns of the CFFF hybrids. CFFF-500, CFFF-600, and CFFF-650 are composed of Fe_3O_4, Fe and FeO (JCPDS card No. 88-0866, No. 87-0721, No. 89-0687, respectively). The Fe content in the CFFF increases with the increase of temperature, while FeO trends in the opposite direction. No FeO phase appears in CFFF-700. Figure 2B exhibits the Raman spectra of the CFFF hybrids. Two characteristic peaks are observed at ~1340 cm^{-1} (D band) and ~1585 cm^{-1} (G band), which confirms the existence of carbon. With the increase of processing temperature, the carbon layer decreases gradually, so the carbon peak becomes less and less obvious. The I_D band is higher than I_G, indicating relatively low graphitization degree of the C layers (Zhou et al., 2020). Two Raman modes at 543 cm^{-1} and 668 cm^{-1} correspond to T_{2gFe-O} and A_{1gFe-O} for the Fe_3O_4, respectively (Liu et al., 2017). The T_{2gFe-O} peaks are ambiguous at the lower processing temperature due to the low crystallinity of Fe_3O_4. Thermogravimetric (TG) analysis of the CFFFs was carried out from 100°C to 800°C at a rate of 10°C·min^{-1}. On heating the obtained samples in an air atmosphere, the CFFF hybrids were finally oxidized to Fe_2O_3 and CO_2 (Figure 2C). The change of weights in the temperature range of 165–520°C are attributed to the oxidation of Fe^0 and Fe^{2+} to Fe^{3+} (Xu et al., 2017). Figure 2D shows the N_2 sorption isotherms of CFFF hybrids. The standard multipoint BET analysis yields a surface area of 41.0, 101, 125, and 35.5 $m^2 \cdot g^{-1}$ for CFFF-500, CFFF-600, CFFF-650, and CFFF-700, respectively. The CFFF-650 samples possess uniformly distributed mesopores centered at about 15 nm (inset, Figure 2D).
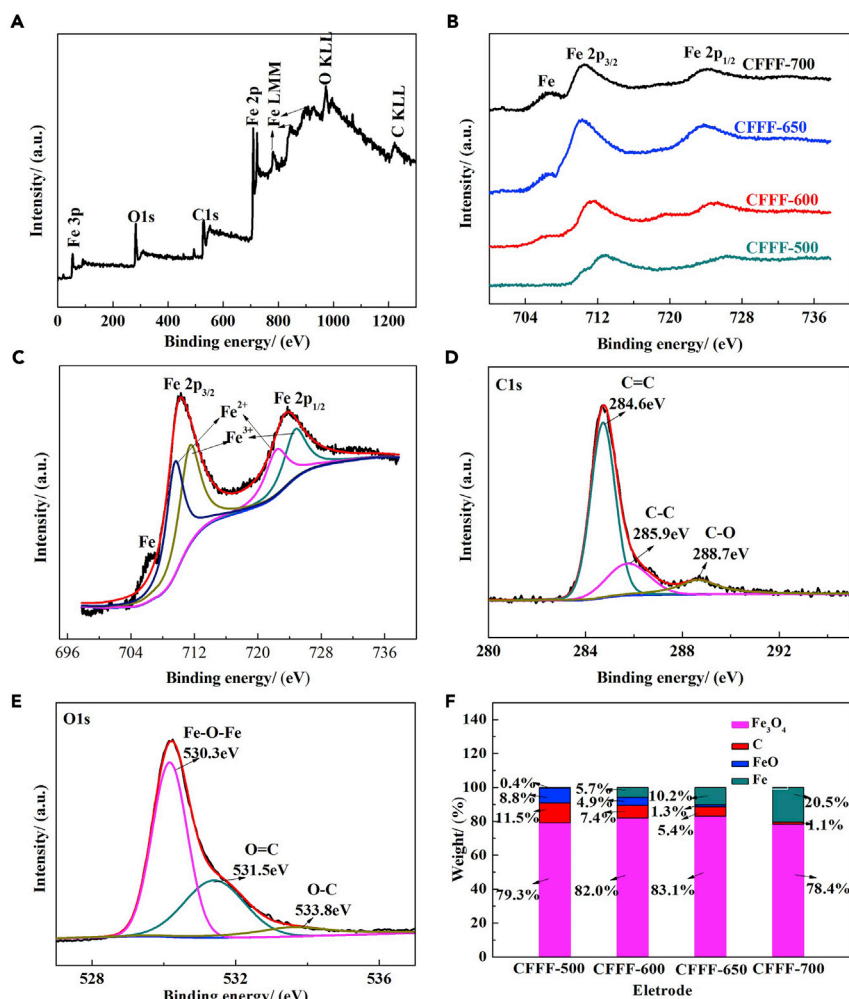
Figure 3. XPS spectra of the CFFF hybrids
(A and E)(A) XPS spectrum, (B) Fe 2p, (C) Fe 2p, (D) C1s and (E) O1s high-resolution spectrum.
(F) The mass fractions of the components of the CFFF hybrids.

X-ray photoelectron spectroscopy (XPS) studies were performed to reveal the surface chemistry of the CFFF hybrids. The full XPS spectrum reveals the existence of C, O, and Fe elements (Figure 3A). In the XPS Fe 2p spectrum (Figure 3B), three peaks are located at about 706.3, 710.3, and 723.8 eV, which are assigned to Fe, Fe $2p_{3/2}$ and Fe $2p_{1/2}$, respectively (Liu et al., 2019). The metallic Fe resulted from the reduction of minor amount of Fe^{2+} and Fe^{3+} by hydrogenation during the solid-state reaction. The peak strength of Fe increases with the increase of temperature, indicating that the content of Fe increases. The peaks of Fe $2p_{3/2}$ and Fe $2p_{1/2}$ can be further deconvolved into four peaks (Figure 3C). Amongst these, the peaks at 709.7 and 722.6 eV represent the binding energy of lattice Fe^{2+}, while the peaks at 711.7 and 724.9 eV are attributed to lattice Fe^{3+} (Grosvenor et al., 2004). The C1s spectrum is fitted into three states with a main sp^2 C peak (284.6 eV), C-O peak (285.9 eV), O-C=O peak (288.7 eV) (Figure 3D). The deconvoluted O1s XPS spectrum exhibits three peaks at 530.3 eV, 531.5 eV, and 533.8 eV, indicating the presence of Fe-O, O=C, and O-C, respectively (Figure 3E).(Li et al., 2021) Figure 3F shows the mass fraction of each component calculated according to the XPS data. Fe_3O_4 is always the dominant component of the CFFF hybrids, along with small amount of FeO and C.

With the increase of the reaction temperature, the percentage of Fe content increases, while those of C and FeO decrease. These XPS results further confirm the formation of mixed valence CFFF hybrids during the thermal pyrolysis, which is consistent with the XRD analysis. As summarized in Table S1, in the synthesis
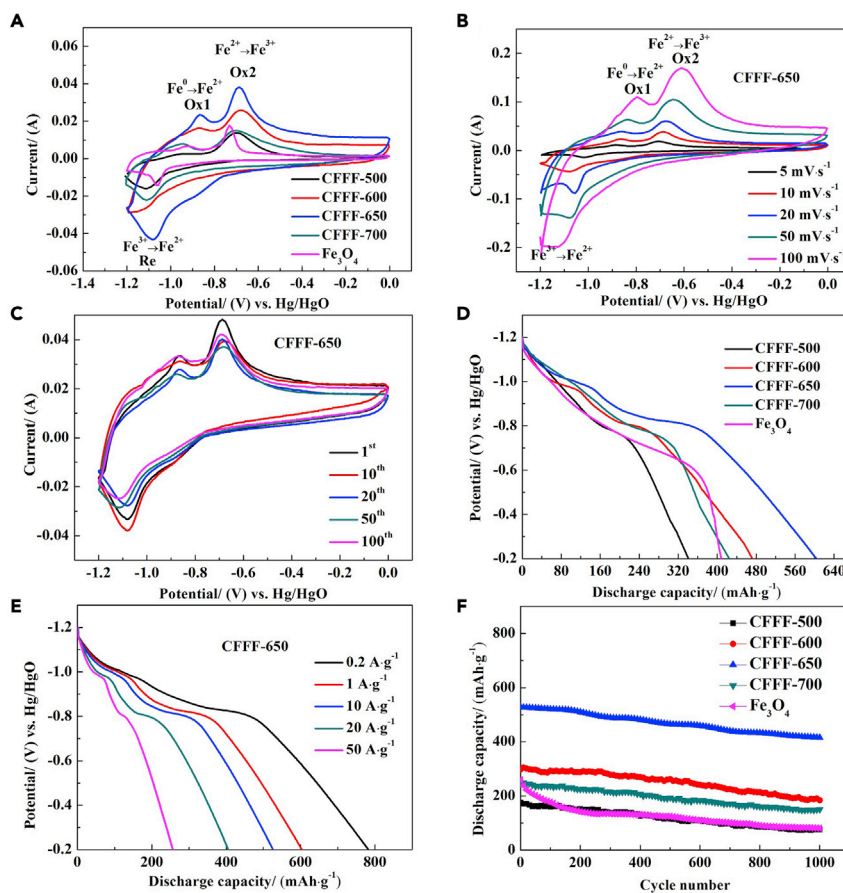
Figure 4. Electrochemical characterization of CFFF hybrids

(A) CV scans at 10 mV·s^{-1} for the CFFF electrodes and Fe_3O_4.

(B) CV plots of CFFF-650 at various scan rates.

(C) Cyclic voltammograms for the CFFF-650 composite for the initial 100 cycles at a scan rate of 10 mV·s^{-1}.

(D) Discharge curves of the CFFF at 1 A·g^{-1}.

(E) Discharge curves of CFFF-650 at different current densities.
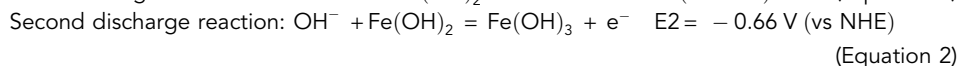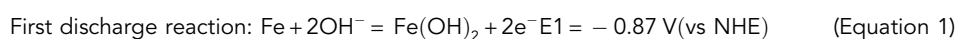
(F) Cycling performance of CFFF electrodes at 10 A·g^{-1}. Electrolyte is an aqueous solution containing 4 M KOH and 2% LiOH.

process, it is expected that there are three reactions of $FeC_2O_4 \cdot 2H_2O$, including a dehydration stage (140–250°C), a decomposition stage (250–400°C) and a reduction stage (400–800°C) (Carles et al., 1999). In a H_2/Ar atmosphere, Fe_3O_4 is the dominant product, accompanied with small amounts of FeO and C. The main reactions include: $3FeC_2O_4 \rightarrow Fe_3O_4 + 4CO + 2CO_2$, $FeC_2O_4 \rightarrow FeO + CO + CO_2$ and $CO + H_2 \rightarrow C + H_2O$. With further increase in temperature, the FeO decomposes into Fe and Fe_3O_4. At 700°C, some Fe_3O_4 is further reduced to Fe. $FeC_2O_4 \cdot 2H_2O$ possesses a six coordinated linear structure, which is beneficial to stabilize the skeleton structure in the reaction process.

## Electrochemical performance of CFFF hybrids

The electrochemical performance of the CFFFs was investigated in 4 M KOH and 2% LiOH electrolyte using a three-electrode testing system. The addition of lithium hydroxide is to protect the positive electrode against migrated ferric hydroxide and improve the long-term durability (Shukla et al., 1994). Nano-Fe_3O_4 was also tested under the same conditions for comparison. Figure 4A displays their respective cyclic voltammetry (CV) curves in a potential window of -1.2 V – 0.0 V at 10 mV·s^{-1}. All the samples exhibit a similar CV profile but different peak positions. The distortion of the CV curves can be observed in the negative scan, which routinely occurs in Ni-Fe batteries due to the interference of underlying hydrogen evolution (Mulder et al., 2017). The redox peaks of CFFF-650 exhibit a much higher intensity than those of the other

CFFF hybrids and nano-Fe_3O_4, revealing that CFFF-650 has the highest activity. Additionally, the CV integral area of the CFFF-650 peaks is larger than those of the other CFFFs and nano-Fe_3O_4, indicating that CFFF-650 also has the highest specific capacity. Two oxidation peaks are observed near −0.87 V (Ox_1) and −0.68 V (Ox_2) in the anodic scan, which are related to the transitions from Fe^0 to Fe^{2+} and from Fe^{2+} to Fe^{3+}(Qin et al., 2020). The peak separation for the Fe^{3+} to Fe^{2+} redox pairs measured on CFFF-650 is ~190 mV, which is lower than those of the CFFF-500 (240 mV), CFFF-600 (220 mV) and CFFF-700 (260 mV) counterparts. This evidences the superior electrochemical kinetics of the CFFF-650 electrode. The peak values for the $Fe^0 \rightarrow Fe^{2+}$ reaction are generally lower than those for the $Fe^{2+} \rightarrow Fe^{3+}$ reaction, indicating a multi-component mixture of the active materials, as confirmed by the XRD patterns after cycling in Figure S6. The similarity of the XRD patterns before and after cycling (Figures 2A and S6) indicate that the electrode material has good stability during electrochemical cycling. During the cathodic scan, due to the interference of hydrogen evolution reaction, the reaction peaks of $Fe^{3+} \rightarrow Fe^{2+} \rightarrow Fe$ are not well defined. Based on the iron-water Pourbaix diagram, interference from the H_2 evolution reaction is expected at potentials below −1.1 V vs Hg/HgO at this pH, limiting the scope to further reduce the material (Jiang et al., 2014). The CFFF-650 continues to provide well-behaved redox activity over scan rates ranging from 5 to 100 mV·s^{-1} (Figure 4B), revealing a good rate capability. The increase of polarization is caused by the increasing scan rate, and the oxidation peaks (Ox) and the corresponding reduction peaks (Re) shift to a more positive value and a more negative value, respectively. The peak shift is quite small, and there is no obvious deformation in CV shape, evidencing high stability and rapid electrochemical dynamics. Using the CV peak currents (I_{ap}), the diffusion process of the electrode can be determined using the Sevick equation. It can be seen that the I_{pa} versus $\upsilon^{1/2}$ plots exhibit a linear relationship (Figure S7), from which it can be reasonably inferred that the oxidation process is diffusion limited (Liu et al., 2014). The plot for the FeO_x-650 electrode (red dotted line) exhibited a steeper slope compared to the electrode fabricated using Fe_3O_4 and the other sample, indicating higher diffusion coefficients and faster electrochemical reactions. Notably, the Re/Ox peak current ratio for the CFFF-650 electrode initially decreases with increasing cycles and then remains nearly constant after 20 cycles (Figure 4C). At a current density of 1 A·g^{-1}, the CFFF-500, CFFF-600, CFFF-650, CFFF-700, and nano-Fe_3O_4 electrodes, possess a specific capacity of 342, 473, 604, 426, and 409 mAh·g^{-1} (Figure 4D), respectively. CFFF-650 clearly exhibits the highest discharge capacity amongst the materials studied. This may be the result of an optimum nano-structure of the material allowing both better electrolyte access via the meso-porosity and shorter internal diffusion distances for the OH^- anions that must participate in the redox process. Figure 4E shows typical discharge curves of the CFFF-650 electrode as a function of rate. The two plateaus on discharge correspond to the formation of the stable +2 and +3 valent states of the iron reaction products. The reaction of the iron electrode, and their standard potentials vs the normal hydrogen electrode (NHE), can be written as:

$$\text{First discharge reaction: } Fe + 2OH^- = Fe(OH)_2 + 2e^- \quad E1 = -0.87 \text{ V(vs NHE)} \qquad \text{(Equation 1)}$$
$$\text{Second discharge reaction: } OH^- + Fe(OH)_2 = Fe(OH)_3 + e^- \quad E2 = -0.66 \text{ V (vs NHE)}$$
$$\text{(Equation 2)}$$

The theoretical capacity for Fe in reactions (1)-(2) is 1278 mAh·g^{-1} (Fe). This indicates that the material utilization in the discharge processes in Figure 4D is still only a fraction of theoretical, no doubt due to incomplete conversion in the core of the nano-particles and also the previously mentioned lack of complete reduction to Fe^0 in the reduction cycle. This also suggests there is scope for further optimization of these materials toward higher utilization. The discharge capacity retention of CFFF-650 was ~96.5% at 1 A·g^{-1} after 100 cycles (Figure S8). At 10 A·g^{-1}, the CFFF-650 exhibits a discharge capacity retention of ~77.3% after 1000 cycles, which is much higher than the CFFF-500, CFFF-600, CFFF-700, and nano-Fe_3O_4 electrodes (Figure 4F). At even higher current densities of 20 and 50 A·g^{-1}, the CFFF-650 can still deliver specific capacities of 407 and 257 mAh·g^{-1}, respectively (Figure 4E), demonstrating an excellent rate capability. It can be inferred that the co-existence of Fe and FeO with Fe_3O_4 can enhance the conductivity and facilitates the redox kinetics. Besides, the nanoconfinement of the carbon layers can effectively restrain the volume expansion of the iron oxide nanocrystals and allow for strong covalent coupling between the iron oxide nanocrystals and the carbon, leading to rapid electron transfer during the electrochemical process.

Figure 5 (a) displays the Nyquist plots obtained for the CFFF and Fe_3O_4 electrodes at 25°C. All the electrodes exhibit a similar shape: a depressed semicircle in the high frequency region (corresponding to the charge-transfer resistance) and a linear region at low-frequency (corresponding to Warburg impedance). The charge-transfer resistance of the electrodes was estimated by using an equivalent circuit (inset
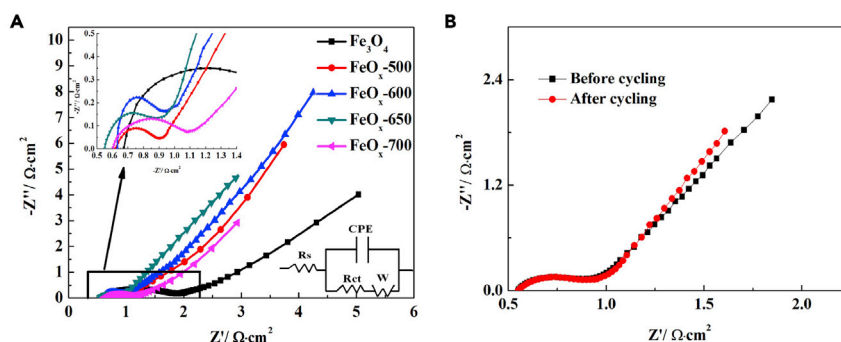
Figure 5. Nyquistplots characterization of electrodes
(A) Nyquist plots of the prepared CFFF electrodes and Fe_3O_4 at the open circuit potential at 25°C.
(B) Nyquist plots of the FeO_x-650 electrodes before (black curve) and after (red curve) 50 charge/discharge cycles.

in Figure 5 (a)) to fit the EIS data. The intercept of the data on the real axis represents the equivalent series total resistance (Rs) (inherent resistance of the active material, the contact resistance between the active material and the current collector, and ionic resistance of the electrolyte). For the semicircle, the diameter represents the charge transfer resistance of the electrodes (Rct), CPE is a double layer capacitance, and W represents the Warburg impedance (Tang et al., 2019). It is found that Rct of the Fe_3O_4 and CFFF electrodes trend as follows: Fe_3O_4 (1.72 $\Omega\cdot cm^2$) > CFFF-700 (1.02 $\Omega\cdot cm^2$) > CFFF-500 (0.94 $\Omega\cdot cm^2$) > CFFF-600 (0.70 $\Omega\cdot cm^2$) > CFFF-650 (0.68 $\Omega\cdot cm^2$). Interestingly, with increasing temperature the charge-transfer resistance of the CFFF-650 electrode becomes lower, suggesting that the surface structure becomes more active toward electron transfer. The slopes for the five electrodes are in the order of CFFF-650 > CFFF-600 > CFFF-500 > CFFF-700 > Fe_3O_4, revealing a diffusion coefficient trend in the same order. The bigger diffusion coefficient, as seen for CFFF-650, should favor faster ion transportation, accelerating electrochemical reaction rates and reducing the polarization in the process of charging and discharging. The obtained CV results are consistent with this. The Nyquist plots of the CFFF-650 electrode before and after cycling also indicate (Figure 5B) the structural integrity of the CFFF-650 electrode. The charge transfer semicircle changed little over the course of 50 charge/discharge cycles (Figure 5B).

Performance evaluation of a CFFF-based Ni-Fe battery

In order to further evaluate the feasibility of CFFF hybrid materials in practical application, the CFFF-650 electrode was used as the anode to assemble Ni-Fe button type batteries (Figure 6A) using a commercial $Ni(OH)_2$ material as cathode. The button cell battery was assembled with a mass ratio of the active materials in the two electrodes of 4.0 (cathode/anode) based on the measured respective specific capacities (cathode capacity estimate from Figure S9). The button type batteries were tested in the voltage window of 0.8 - 1.6 V at room temperature. Figure 6B shows two Ni-Fe button batteries connected in series readily operating a light-emitting diode (LED, ~2.0 V, 10–20 mA). The output current was 15.3 mA at the beginning and 11.3 mA after 6 hr. Even after 10 hr, the LED was still on and the output current remained at 10.1 mA, exhibiting an excellent durability. Figure 6C shows the Ragone plot of the Ni-Fe button battery compared with other aqueous energy storage systems. The Ni-Fe button battery is capable of outputting a specific energy of 127 and 110 Wh·kg^{-1} at a power density of 0.58 and 5.07 kW·kg^{-1}, respectively (masses used here include anode, cathode separator, electrolyte and casing). When evaluated under a maximum power density of 34.1 kW·kg^{-1}, the Ni-Fe battery still maintains a satisfactory energy density of 61.4 Wh·kg^{-1}. The error estimates for the power density and energy density are ~5%. Compared to the traditional Ni-Fe battery and other recent literature, the CFFF-650 electrode-based Ni-Fe battery in this work has both high gravimetric energy density and high rate capability, outperforming the previously reported aqueous rechargeable batteries and supercapacitors(Xia et al., 2015, 2016; Liu et al., 2014; Wang et al., 2017; Song et al., 2018; Ma et al., 2019). Furthermore, the Ni-Fe battery exhibits capacity retention of 89.7% and coulombic efficiency of ~98.5% after 2500 cycles at 300 mA·g^{-1} (Figure 6D); the capacity decay is approximately linear at a rate of 0.0041% per cycle. Projecting this to the usual end of life definition in the battery industry of 70% capacity remaining indicates an estimated lifetime at 300 mA·g^{-1} of more than 7000 cycles. No detectable deformation or expansion was observed on the button cell. The process involved in this slow capacity decay may be related to the slow deterioration of the contact between the active material particles and the conductive carbon and/or the current collector.
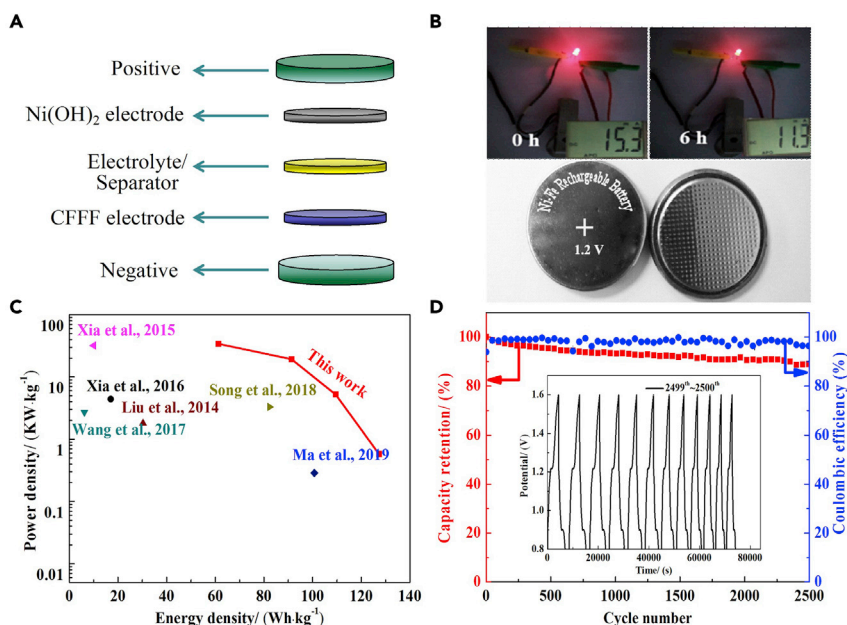
Figure 6. Electrochemical characterization of a CFFF-650 electrode based Ni-Fe button cell

(A) Schematic illustration of device configuration.

(B) Photograph of a red LED indicator powered by two Ni-Fe button batteries at the beginning (top left inset) and after 6 hr (top right inset).

(C) Ragone plot comparing the Ni-Fe button battery compared to the literature (note that the masses used are of whole batteries including the casing).

(D) Cycling stability and Coulombic efficiency at a rate of 300 mA·g^{-1}. The inset shows the galvanostatic charge/discharge curves of the Ni-Fe battery for the last 10 cycles.

DISCUSSION

Mesostructured quaternary carbon/Fe/FeO/Fe$_3$O$_4$ hybrid materials with controlled composition have been successfully synthesized by a one-step solid-state reaction. The excellent performance of the CFFF-650 electrode-based Ni-Fe cells in this work results from the rational design of the composition of the material, which enables a highly efficient utilization of active materials and suppresses the self-discharge and hydrogen evolution in the battery. The composition and valence state of the iron materials is shown to significantly affect their electrochemical performance. Particularly, ultrathin carbon layers formed on iron oxide can improve the chemical stability and inherent conductivity of the FeO$_x$ nanoparticles, inhibiting self-discharge and suppressing the volume changes of iron oxide particles during cycling; hence the cyclability performance and the charge capacity are much improved. The three-dimensional porous framework can also provide extremely large surface area and accommodate the strain or volume change during charge-discharge cycles. Therefore, CFFF hybrids can be utilized as a high capacity and durable electrode material not only for the Ni-Fe battery but also for other electrochemical energy storage devices. The fabrication process is not inherently mass limited and can be easily scaled up. The high performance of this Ni-Fe battery technology has great potential for application in renewable energy stationary storage systems, and we anticipate that Ni-Fe batteries having environmentally friendly, safe, and long life characteristics will offer important advantages in other energy conversion and storage applications.

Limitations of the study

Our work demonstrates a simple approach for the fabrication of quaternary carbon/Fe/FeO/Fe$_3$O$_4$ hybrids with controllable composite properties. The performance of the hybrid can be further optimized. At the current stage, both yield of product and the mass loading of the electrodes in the battery are relatively low. Further scale-up is required in order to increase the capacity of the battery for practical applications.

STAR★METHODS

Detailed methods are provided in the online version of this paper and include the following:

SUPPLEMENTAL INFORMATION

Supplemental information can be found online at https://doi.org/10.1016/j.isci.2021.102547.

AUTHOR CONTRIBUTIONS

X.Z. and D.M. conceived the experiments. Y.Z. and X.M. performed the experiments. X.Z., P.S., and D.M. contributed to the interpretation of experiments. Y.Z., X.Z., and D.M. prepared the manuscript. All the authors discussed the results and commented on the manuscript.

DECLARATION OF INTERESTS

The authors declare no competing interests.

REFERENCES

Carles, V., Alphonse, P., Tailhades, P., and Rousset, A. (1999). Study of thermal decomposition of FeC$_2$O$_4$·2H$_2$O under hydrogen. Thermochim. Acta 334, 107–113.

Chakkaravarthy, C., Periasamy, P., Jegannathan, S., and Vasu, K.I. (1991). The nickel/iron battery. J. Power Sourc. 35, 21–35.

Grosvenor, A.P., Kobe, B.A., Biesinger, M.C., and Mcintyre, N.S. (2004). Investigation of multiplet splitting of Fe 2p XPS spectra and bonding in iron compounds. Surf. Interf. Anal. 36, 1564–1574.

Guo, C.X., and Li, C.M. (2017). Molecule-confined FeO$_x$ nanocrystals mounted on carbon as stable anode material for high energy density nickel-iron batteries. Nano Energy 42, 166–172.

Guo, C.X., Wang, M., Chen, T., Lou, X.W., and Li, C.M. (2011). A hierarchically nanostructured composite of MnO$_2$/conjugated polymer/graphene for high-performance lithium ion batteries. Adv. Energy Mater. 1, 1–6.

Han, C.G., Zhu, C., Sheng, N., Aoki, Y., Habazaki, H., and Akiyama, T. (2017). A facile one-pot synthesis of FeO$_x$/carbon/graphene composites as superior anode materials for lithium-ion batteries. Electrochim. Acta 235, 88–97.

Hariprakash, B., Martha, S.K., Hegde, M.S., and Shukla, A.K. (2005). A sealed, starved-electrolyte nickel-iron battery. J. Appl. Electrochem. 35, 27–32.

Janoschka, T., Martin, N., Martin, U., Friebe, C., Morgenstern, S., Hiller, H., Hager, M.D., and Schubert, U.S. (2015). An aqueous, polymer-based redox-flow battery using non-corrosive, safe, and low-cost materials. Nature 527, 78–81.

Jiang, W., Liang, F., Wang, J., Su, L., Wu, Y., and Wang, L. (2014). Enhanced electrochemical performances of FeO$_x$-graphene nanocomposites as anode materials for alkaline nickel-iron batteries. RSC Adv. 4, 15394–15399.

Lei, D., Lee, D.C., Zhao, E., Magasinski, A., Jung, H.R., Berdichevsky, G., Steingart, D., and Yushin, G. (2018). Iron oxide nanoconfined in carbon nanopores as high capacity anode for rechargeable alkaline batteries. Nano Energy 48, 170–179.

Li, J., Wang, S., Chen, X., Xiao, T., Tan, X., Xiang, P., and Jiang, L. (2018). Enhancing electrochemical performance of Fe$_2$O$_3$ via in situ sulfurization and carbon coating modification for nickel-iron rechargeable batteries. Electrochim. Acta 290, 332–338.

Li, L., Zhu, J., Niu, Y., Xiong, Z.H., and Jiang, J. (2017). Metallic Fe nanoparticles trapped in self-adapting nanoreactors: a novel high-capacity anode for aqueous Ni-Fe batteries. Chem. Commun. 53, 12661–12664.

Li, X., Yang, X., Ye, J., Xia, G., and Hu, C. (2021). A trifunctional modified separator based on Fe tetraaminophthalocyanine@rGO for lithium-sulfur batteries. Chem. Eng. J. 405, 126947.

Liu, X., Yang, Q., Mi, M., Kong, W., and Hu, J. (2019). Fe1-xS/reduced graphene oxide composite as anode material for aqueous rechargeable Ni/Fe batteries. J. Alloys Compd. 800, 99–106.

Liu, B.T., Zhao, M., Han, L.P., Lang, X.Y., Wen, Z., and Jiang, Q. (2017). Three-dimensional nanoporous N-doped graphene/iron oxides as anode materials for high-density energy storage in asymmetric supercapacitors. Chem. Eng. J. 335, 467–474.

Liu, J., Chen, M., Zhang, L., Jiang, J., Yan, J., Huang, Y., Lin, J., Fan, H.J., and Shen, Z.X. (2014). A flexible alkaline rechargeable Ni/Fe battery based on graphene foam/carbon nanotubes hybrid film. Nano Lett. 14, 7180–7187.

Ma, J., Guo, X., Yan, Y., Xue, H., and Pang, H. (2018). FeO$_x$-based materials for electrochemical energy storage. Adv. Sci. *5*, 1700986.

Ma, L., Xu, Y., Liu, Y., Zhang, H., and Jiang, J. (2019). Smart colloid-assisted technique prompts the evolution of bamboo wastes into nanometal-inlaid carbon microfibers for sustainable Ni-Fe batteries. ACS Sustain. Chem. Eng. *2019*, 17919–17928.

Mulder, F.M., Weninger, B.M.H., Middelkoop, J., Ooms, F.G.B., and Schreuders, H. (2017). Efficient electricity storage with a battolyser, an integrated Ni-Fe battery and electrolyser. Energy Environ. Sci. *10*, 756–764.

Narayanan, S.,R., Manohar, A.K., and Yang, C.G. (2017). A high-performance sintered iron electrode for rechargeable alkaline batteries to enable large-scale energy storage. J. Electrochem. Soc. *164*, A418–A429.

Qin, Z., Song, Y., Shi, H.Y., Li, C., and Liu, X.X. (2020). Heterojunction induced activation of iron oxide anode for high-power aqueous batteries. Chem. Eng. J. 125874.

Rustomji, C.S., Yang, Y., Kim, T.K., Mac, J., Kim, Y.J., Caldwell, E., Chung, H., and Meng, S. (2017). Liquefied gas electrolytes for electrochemical energy storage devices. Science *356*, 1351.

Shukla, A.K., Ravikumar, M.K., and Balasubramanian, T.S. (1994). Nickel/iron batteries. J. Power Sourc. *51*, 29–36.

Shukla, A.K., Venugopalan, S., and Hariprakash, B. (2001). Nickel-based rechargeable batteries. J. Power Sourc. *100*, 125–148.

Song, Y., Lu, X., Deng, P., Hu, W., Sun, Z., Liu, X.X., and Sun, X. (2018). Morphology engineering of electro-deposited iron oxides for aqueous rechargeable Ni/Fe battery applications. Chem. Eng. J. *354*, 672–679.

Sun, H., Mei, L., Liang, J., Zhao, Z., Lee, C., Fei, H., Ding, M., Lau, J., Li, M., and Wang, C. (2017). Three-dimensional holey-graphene/niobia composite architectures for ultrahigh-rate energy storage. Science *356*, 599–604.

Tang, H., Sun, Z., Chang, K., Hou, Y., Li, B., Hou, Y., and Chang, Z. (2019). Uniform carbon coating drastically enhances the electrochemical performance of a Fe$_3$O$_4$ electrode for alkaline nickel-iron rechargeable batteries. Int. J. Hydrogen Energy *44*, 24895–24904.

Wang, H., Liang, Y., Gong, M., Li, Y., Chang, W., Mefford, T., Zhou, J., Wang, J., Regier, T., and Wei, F. (2012). An ultrafast nickel-iron battery from strongly coupled inorganic nanoparticle/nanocarbon hybrid materials. Nat. Commun. *3*, 917.

Wang, P., Pu, Z., Li, Y., Wu, L., and Mu, S. (2017). Iron-doped nickel phosphide nanosheet arrays: an efficient bifunctional electrocatalyst for water splitting. ACS Appl. Mater. Interfaces *9*, 26001–26007.

Wang, X., Ding, R., Ren, X., Shi, L., Li, Q., Yang, Y., Wang, H., Wang, M., Wang, L., and Lv, B. (2019). Micron iron oxide particles with thickness-controllable carbon coating for Ni-Fe battery. Electrochim. Acta *299*, 800–808.

Weinrich, H., Gehring, M., Tempel, H., Kungl, H., and Eichel, R.A. (2018). Impact of the charging conditions on the discharge performance of rechargeable iron-anodes for alkaline iron-air batteries. J. Appl. Electrochem. *48*, 451–462.

Wu, X., Qi, Y., Hong, J.J., Li, Z., Hernandez, A.S., and Ji, X. (2017). Rocking-chair ammonium-ion battery: a highly reversible aqueous energy storage system. Angew. Chem. Int. Ed. Engl. *56*, 13026–13030.

Xia, H., Hong, C., Li, B., Zhao, B., Lin, Z., Zheng, M., Savilov, S.V., and Aldoshin, S.M. (2015). Facile synthesis of hematite quantum-dot/functionalized graphene-sheet composites as advanced anode materials for asymmetric supercapacitors. Adv. Funct. Mater. *25*, 627–635.

Xia, Q., Xu, M., Xia, H., and Xie, J. (2016). Nanostructured iron oxide/hydroxide-based electrode materials for supercapacitors. ChemNanoMat *2*, 588–600.

Xu, Z.L., Yao, S., Cui, J., Zhou, L., and Kim, J.K. (2017). Atomic scale, amorphous FeO$_x$/carbon nanofiber anodes for Li-ion and Na-ion batteries. Energy Storage Mater. *8*, 10–19.

Zhang, H., Liu, Y., Meng, T., Ma, L., Zhu, J., Xu, M., Li, C.M., Zhou, W., and Jiang, J. (2019). Mass production of metallic Fe@carbon nanoparticles with plastic and rusty wastes for high-capacity anodes of Ni-Fe batteries. ACS Sustain. Chem. Eng. *7*, 10995–11003.

Zhou, M., Yang, B., Zhao, Y., Jin, Z., and Cai, Z. (2020). Facile preparation of N-doped carbon/FeO$_x$-decorated carbon cloth for flexible symmetric solid-state supercapacitors. Cellulose *27*, 1–11.

STAR★METHODS

KEY RESOURCES TABLE

REAGENT or RESOURCE	SOURCE	IDENTIFIER
Chemicals, peptides, and recombinant proteins		
Ferrous oxalate (99%, Alfa)	Aladdin	CAS#6047-25-2
sodium bicarbonate (≧99.8%, AR)	Aladdin	CAS#144-55-8
Potassium hydroxide (90%, AR)	Aladdin	CAS#1310-58-3
Lithium hydroxide (98%, AR)	Aladdin	CAS#1310-65-2
Iron oxide(II,III) (50-100 nm)	Aladdin	CAS#1317-61-9
Acetylene black (300 mesh)	Macklin	CAS#1333-86-4
Carboxyl methyl cellulose (Mw~90000)	Aladdin	CAS#9004-32-4
Polytetrafluoroethylene (25μm)	Aladdin	CAS#9002-84-0
$Ni(OH)_2$	Macklin	CAS#12054-48-7
Critical commercial assays		
Platinum (Pt) electrode	Shanghai yueci Electronic Technology Co., Ltd	PT252
Mercury/mercuric oxide electrode	Shanghai yueci Electronic Technology Co., Ltd	R502
Battery case	Neware, China	CR2032
Deposited data		
XRD PDF# data	MDI Jade 5	JCPDS 72-1193
Software and algorithms		
Zennium Electrochemical Workstation	Zahner, Germany	https://www.chem17.com/product/detail/814811.html
LAND Ct2001A	Neware, China	https://www.neware.com.cn/
Origin.8	http://www.OriginLab.com	GF3S4-9089-7123456
Other		
Field Emission Scanning Electron Microscopy	SU 8220, Hitachi, Japan	https://www.instrument.com.cn/
Transmission Electron Microscopy	G2 ETEM, Titan, USA	https://www.instrument.com.cn/
X-ray photoelectron spectroscopy	ESCALAB MK II XPS	https://www.chem17.com/
X-ray diffraction	SMARTLAB3KW, Japan	https://www.chem17.com/
Raman spectra	Horiba Lab RAM HR	https://www.instrument.com.cn/
Thermogravimetry	STA 449 F5, Germany	https://www.instrument.com.cn/
Brunauer-Emmett-Teller	Micromeritics, ASAP 2460 HD88	https://www.chem17.com/

RESOURCE AVAILABILITY

Lead contact

Further information and requests for resources should be directed to and will be fulfilled by the lead contact: Douglas R. Macfarlane (douglas.macfarlane@monash.edu).

Materials availability

This study did not generate new unique reagents.

Data and code availability

This study did not generate any datasets.

METHOD DETAILS

Synthesis of CFFF hybrids

$FeC_2O_4 \cdot 2H_2O$ (1g) was dispersed in the mixture of deionized water and ethanol containing a pore-forming agent (50 mg $NaHCO_3$). The mixture was dried in vacuum at 100°C overnight, and the products were kept in a tubular furnace in a mixture of 5% H_2 and 95% Ar atmosphere at 500°C, 600°C, 650°C or 700°C. In the process of thermal decomposition, the heating rate was 5°C·min⁻¹, the airflow rate was 20 mL·min⁻¹, and the decomposition time was 30 min. The products were centrifuged off, washed with ethanol and deionized water five times alternately, and dried at 60°C in vacuum. They are named as CFFF-500, CFFF-600, CFFF-650 and CFFF-700, respectively.

Sample characterization

Morphology and structure of the materials were investigated by field emission scanning electron microscopy (FESEM, SU 8220, Hitachi, Japan), and transmission electron microscopy (TEM & HRTEM, G2 ETEM, Titan, USA). The crystal structure was characterized by X-ray diffraction (XRD, SMARTLAB3KW, Japan) using Cu Kα radiation. Raman spectra were recorded on a Horiba Lab RAM HR Evolution spectrometer using a 514 nm argon ion laser. X-ray photoelectron spectroscopy (XPS) measurement was performed on an ESCALAB MK II XPS spectrometer to analyze the surface composition, using monochromatic Al Kα X-rays. Compositions were determined by thermogravimetry (TGA, STA 449 F5, Germany). During the TG measurement, the samples were heated from 100°C up to 800°C at a heating rate of 10°C·min⁻¹ in a dynamic atmosphere of air using α-alumina crucibles. The surface area was measured by nitrogen physisorption (Micromeritics, ASAP 2460 HD88) based on the Brunauer-Emmett-Teller (BET) method. The specific surface area of the samples was calculated following the multipoint BET procedure.

Preparation of CFFF anodes and electrochemical measurements

The CFFF anodes were prepared by mixing 90% CFFF, 6% acetylene black, 2% carboxyl methyl cellulose (CMC) and 2% polytetrafluoroethylene (PTFE), and then dispersing in ethanol and deionized water under stirring for 2 h, resulting in a concentration of 1 mg·mL⁻¹ in the slurry material. The mixture was painted onto 1.5×1.5 cm nickel plated perforated steel strip and dried at 100°C in vacuum; from this an electrode of 3 mm thickness was obtained by pressing with a roller press. All the CFFF electrodes were prepared following the above procedures unless otherwise noted. Electrochemical measurements were performed on a Zennium Electrochemical Workstation using a three-electrode configuration, where mercury/mercuric oxide (vs. Hg/HgO) was used as the reference electrode (E_0 = +0.098 V vs. the NHE) and platinum (Pt) electrode as the counter electrode. A solution containing 4 M KOH and 2% LiOH was used as the electrolyte.

Fabrication and measurement of Ni-Fe button batteries

In order to demonstrate the practical application of CFFFs, Ni-Fe button batteries (CR2032) were fabricated in a two-electrode configuration with a CFFF-650 based anode and a home-made sintered $Ni(OH)_2$ cathode. The CFFF-650 anodic materials were made from 90% CFFF-650, 6% acetylene black, 2% carboxyl methyl cellulose (CMC) and 2% polytetrafluoroethylene (PTFE). The cathode electrodes were comprised of commercial sintered $Ni(OH)_2$, acetylene black, and polytetrafluoroethylene (PTFE) at a weight ratio of 8:1:1. The two electrodes were pasted on titanium foil using distilled water and ethanol as the solvent and dried at 100°C in vacuum for 3h. Then, the positive and negative plates were cut into circular plates with diameters of 16 and 14 mm, with aerial active material loading of 4-4.5 and 1.0-1.2 mg·cm⁻², respectively. The two electrodes were separated by a microporous polypropylene membrane soaked in 4 M KOH and 2% LiOH solution. Galvanostatic cycling experiments of the Ni-Fe cells were performed on an LAND Ct2001A battery test system at the voltage window of 0.8-1.6 V at room temperature.

Discharge specific capacity (C, mAh·g⁻¹) of active materials was calculated from discharge profiles at different current densities using the equation: $C = I \times \Delta t/m$, where I, Δt and m are the discharge current density (A), discharge time (s), and mass of the active material mass (g). Energy density E (Wh·kg⁻¹) and power density P (W·kg⁻¹) of the coin cell devices were calculated from:

$$E = I \int_0^{\Delta t} V(t)dt \Big/ m \qquad \text{(Equation 3)}$$

$$P = E/\varDelta t \qquad \text{(Equation 4)}$$

where I is discharging current, V is discharging voltage, dt is time differential, and $\varDelta t$ is the discharge time. In this case, m is taken as the total mass of the anode, cathode, membrane and electrolyte in the device.